

Effects of grain size and boundary structure on the dynamic tensile response of copper

J. P. Escobedo,¹ D. Dennis-Koller,^{2,a)} E. K. Cerreta,¹ B. M. Patterson,³ C. A. Bronkhorst,⁴ B. L. Hansen,⁴ D. Tonks,⁵ and R. A. Lebensohn¹

¹MST-8, Los Alamos National Laboratory Los Alamos, New Mexico 87544, USA

²WX-9, Los Alamos National Laboratory Los Alamos, New Mexico 87544, USA

³MST-7, Los Alamos National Laboratory Los Alamos, New Mexico 87544, USA

⁴T-3, Los Alamos National Laboratory Los Alamos, New Mexico 87544, USA

⁵XCP-5, Los Alamos National Laboratory Los Alamos, New Mexico 87544, USA

(Received 1 February 2011; accepted 2 June 2011; published online 5 August 2011)

Plate impact experiments have been carried out to examine the influence of grain boundary characteristics on the dynamic tensile response of Cu samples with grain sizes of 30, 60, 100, and 200 μm . The peak compressive stress is ~ 1.50 GPa for all experiments, low enough to cause an early stage of incipient spall damage that is correlated to the surrounding microstructure in metallographic analysis. The experimental configuration used in this work permits real-time measurements of the sample free surface velocity histories, soft-recovery, and postimpact examination of the damaged microstructure. The resulting tensile damage in the recovered samples is examined using optical and electron microscopy along with micro x-ray tomography. The free surface velocity measurements are used to calculate spall strength values and show no significant effect of the grain size. However, differences are observed in the free surface velocity behavior after the pull-back minima, when reacceleration occurs. The magnitude of the spall peak and its acceleration rate are dependent upon the grain size. The quantitative, postimpact, metallographic analyses of recovered samples show that for the materials with grain sizes larger than 30 μm , the void volume fraction and the average void size increase with increasing grain size. In the 30 and 200 μm samples, void coalescence is observed to dominate the void growth behavior, whereas in 60 and 100 μm samples, void growth is dominated by the growth of isolated voids. Electron backscatter diffraction (EBSD) observations show that voids preferentially nucleate and grow at grain boundaries with high angle misorientation. However, special boundaries corresponding to $\Sigma 1$ (low angle, $< 5^\circ$) and $\Sigma 3$ ($\sim 60^\circ$ $\langle 111 \rangle$ misorientation) types are more resistant to void formation. Finally, micro x-ray tomography results show three dimensional (3D) views of the damage fields consistent with the two dimensional (2D) surface observations. Based on these findings, mechanisms for the void growth and coalescence are proposed. © 2011 American Institute of Physics. [doi:10.1063/1.3607294]

I. INTRODUCTION

Material performance in extreme environments, such as high pressure, high strain and high strain-rate, is of scientific interest because it involves a wide spectrum of issues ranging across defense and industrial applications. Shock compression via plate impact is often used to investigate dynamic damage processes because of the ability to control global one-dimensional, planar strain loading conditions and to recover the sample for metallurgical analysis. In a plate impact experiment, dynamic tensile damage occurs when rarefaction (decompression) waves within the target material interact to produce tensile stresses in excess of the yielding threshold required for damage initiation.¹

If tensile stresses within a ductile material are high, damage (in the form of voids) will nucleate, grow and coalesce; ultimately forming a failure plane within the material termed a “spall layer.” Evidence that such damage has been created in a plate impact experiment is often obtained using

a velocity interferometer system for any reflector (VISAR)² or a photon Doppler velocimetry (PDV) system.^{3–5} In general, the free surface velocity profile obtained using VISAR or PDV reveals ringing consistent with wave reflections within a region of material thinner than the original sample. If tension developed within the target material during the experiment is not sufficient to cause complete separation, a damage field - termed “incipient spallation” —may form. This region is typically of lower impedance than the undamaged material and can produce a free surface velocity profile similar or even identical to that obtained from a completely spalled sample. Therefore, sample recovery and metallographic analyses are utilized to determine the damage state.

Extensive work to date has established that spall is a complex process strongly influenced by the dynamic loading profile or shock wave shape imparted to the specimen.^{6–8} However, while this is now generally accepted, the influence of the individual characteristics of the shock wave shape on damage evolution is not well understood. These characteristics include rise time, pulse duration, peak shock stress (compressive and tensile) and release rate. In addition, as the shock wave shape is altered experimentally, one important

^{a)}Author to whom correspondence should be addressed. Electronic mail: ddennis@lanl.gov.

parameter that is frequently unaddressed is the coupling of that changing shock wave shape to the changes in the volume of material that is subjected to tension during a dynamic experiment. Figure 1 illustrates the effect of changes in shock wave shape (resulting from changes in impactor and target geometry) on the characteristics of the region of tension developed in the material leading to damage. Changes in pulse shape that significantly effect the volume of material being sampled in tension⁹ are believed to couple with microstructural length scales in a specimen to yield changes in the damage observed in soft recovered flyer plate experiments. To address this, a study has been performed aimed at experimentally decoupling kinetics effects from spatial effects (microstructural defect distributions) imparted on a specimen as a function of shock wave shape. As a first step, in this study controlled incipient spall experiments were performed to assess the role of defect distribution in damage evolution. In this first piece of the study, the loading condition (shock wave shape) and the volume of material subjected to tension, was carefully controlled and held constant.

The effect of the microstructure on the spall (damage) response has been studied extensively. The body of literature spans from the classic works by Barbee, Curran and Seaman,^{10–12} to Meyers *et al.*,¹³ Gray *et al.*,^{6–8} and recently by Minich *et al.*,^{14–16} among many others.^{17–19} However, most of the cited work has focused on the effects of microstructure on pull-back measurements in experiments in which the sample experienced complete failure. In this scenario, many parameters and mechanisms (i.e., shock hardening, void nucleation, growth, and coalescence) are intertwined. This

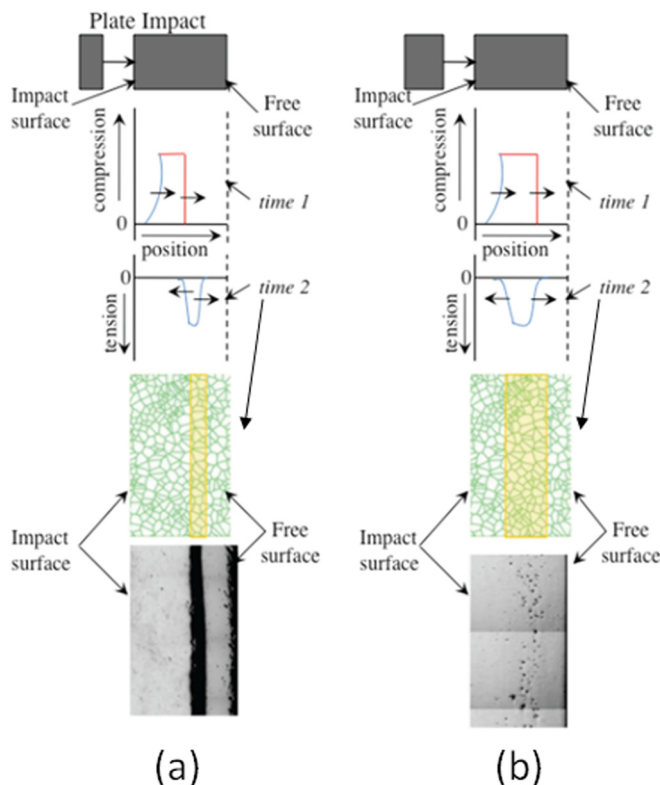


FIG. 1. (Color online) Wave shape affects the volume under tension, causing different damage fields: (a) narrow/localized = complete spall, (b) wide/spread = incipient spall.

precludes any significant conclusion about the individual contributions of material characteristics and kinetics of loading from these measurements. For instance, the effect of the grain size has shown contradictory results, some studies have found a Hall–Petch-type of relationship,²⁰ while others have found the opposite, the calculated spall strength increases with increasing grain size.^{14,21}

Moreover, the evolution of more subtle plastic processes leading to incipient cracking or void formation in a material has not been fully addressed and therefore is not adequately captured by existing damage models.^{22–25} Recent investigations suggest that a physical basis to track the microstructural evolution of plasticity leading to early stage damage may be necessary to accurately predict dynamic failure of high purity metals.²⁶ This is the main objective addressed in this study: To elucidate fundamental mechanisms of void nucleation, growth, and coalescence for specific microstructural details. To this end, incipient spall experiments are performed on high-purity copper samples with a known grain boundary density/distribution (grain size) to examine the relationship between these defect characteristics and void growth. Characterization of the resultant damage is performed via standard optical and electron backscatter diffraction (2D) analyses, along with micro x-ray tomography (3D).

II. EXPERIMENTAL METHODS

A. Initial material characterization

All target materials were prepared from fully annealed 99.999% pure oxygen-free high-conductivity (OFHC) copper and have the same pedigree as the samples used in one of our earlier studies,²⁷ in which the quasi-static compressive yield strength of copper revealed a very weak grain size dependency (< 5 MPa). The samples have average grain sizes of 30, 60, 100, and 200 μm following annealing under vacuum at 450 $^{\circ}\text{C}$ for 30 min., 600 $^{\circ}\text{C}$ for 1 h, 850 $^{\circ}\text{C}$ for 1 h, and 900 $^{\circ}\text{C}$ for 35 min, respectively. The grain size is estimated by using the intercept method in combination with automated analysis of electron backscatter diffraction (EBSD) data in which twin boundaries are not included.

Figures 2(a)–2(d) show the initial characterization of the four microstructures tested. The figure contains orientation maps along with respective pole figures and misorientation distributions. It is observed that the 30, 60, and 100 μm samples possess a weak texture, 2 to 3 times that of a random texture. In addition, EBSD data reveals that the total grain boundary length divided by the respective area characterized decreases with increasing grain size. The average values were calculated to be ~ 1.5 , 1.4, and 1.3 [$1/\mu\text{m}$] with twins and ~ 0.031 , 0.027, 0.026 [$1/\mu\text{m}$] excluding twins, for the 30, 60, and 100 μm samples, respectively. It should be noted that not only was the defect density/distribution (grain boundary) strictly controlled, but the defect nature (grain boundary type) was, as well. The fraction of boundaries with misorientations of $\sim 39^{\circ}$ or 60° , that fulfill the special $\Sigma 9$ and $\Sigma 3$ boundary criteria, were held to similar values for all cases (a total fraction of ~ 0.7). The only exception was the 200 μm sample which shows a higher fraction of $\Sigma 3$, slightly higher texture strength, and lower grain boundary length

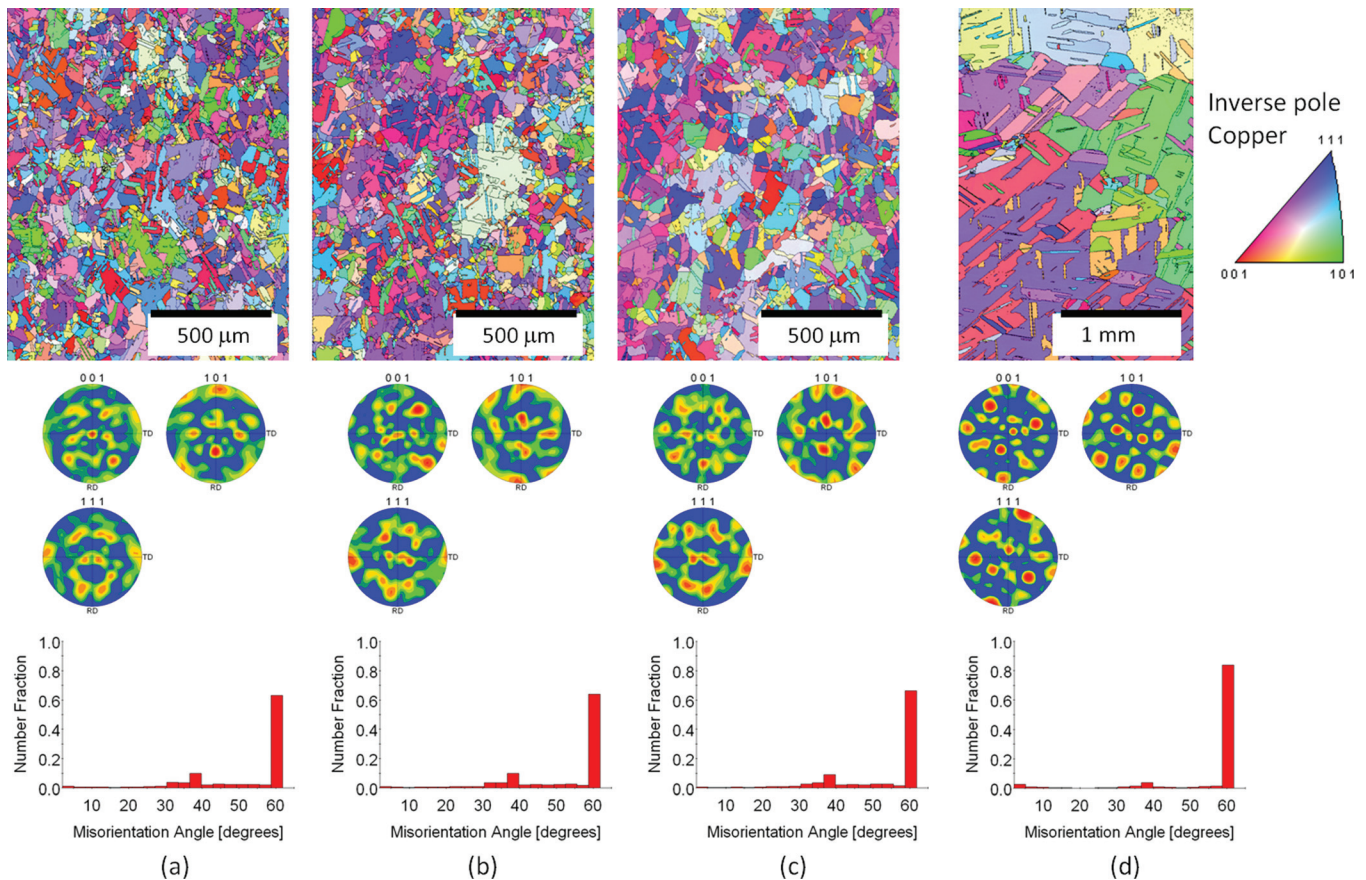


FIG. 2. (Color) Microstructures tested: (a) 450°C – 30 min (30 μm), (b) 600°C – 1 h (60 μm), (c) 850°C – 1 h (100 μm), (d) 900°C – 35 min (200 μm).

densities (0.027 with twins and 0.026 [$1/\mu\text{m}$] without twins). These results may be readily explained in terms of the lower number of grains analyzed in this case. In all cases, the textures and misorientation distributions are consistent with those typically obtained in recrystallized copper.

B. Plate impact experiments

Plate impact experiments have been conducted using a smooth bore 78 mm light gas gun. Figure 3 shows a schematic of the experimental configuration used. A single well characterized loading condition is chosen for all experiments to ensure the kinetic aspects of the tensile stress profile evo-

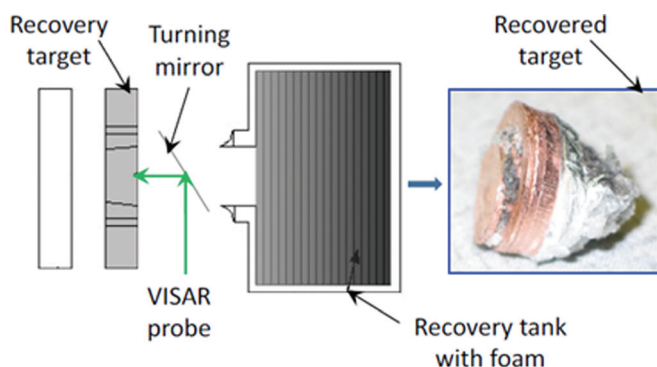


FIG. 3. (Color) Experimental configuration used for soft recovery experiments with VISAR diagnostics.

lution remain consistent for all experiments. The length scale parameters (in the form of grain size) are altered by changing the number of grain boundaries subjected to the tensile stress profile. Quartz impactors (z -cut, 2 mm nominal thickness) are mounted on Lexan sabots and launched using Ar gas. Quartz impactors ensure that a single, elastic shock wave is produced in the stress range of interest to this study. Table I lists the experimental details (stress calculations are discussed in the next section). To ensure that the recovered samples are subjected to only a known uniaxial loading/unloading history, significant radial release is minimized. Typically, this is accomplished by placing rings made of the same material — termed “momentum trapping rings”—around the sample. If properly designed, the rarefaction release wave relieves the stress to zero in the sample uniaxially and the sample separates from the rings before the radial release waves reach it. This technique of momentum trapping is described elsewhere²⁸ and has proven effective in mitigating radial release in numerous experiments. Finite difference calculations by Stevens and Jones²⁹ demonstrate that if radial release is not mitigated, the plastic work in the sample may be up to a factor of 10 higher than that resulting from only uniaxial loading/unloading.

1. Target preparation

Using the general relationship given by Gray *et al.*,³⁰ a single momentum ring, approximately 12 mm wide is needed

TABLE I. Experimental parameters for the plate impact experiments.

Experiment No.	Experiment		Impactor			Sample thickness (mm)	Peak velocity V_{pk} (m/s)	Compressive stress (GPa)
	Shot ID	Grain size (μm)	Material	Thickness (mm)	Velocity (m/s)			
1	1s-1430	30	z-cut quartz	2.027	134	3.998	84	1.50
2	1s-1440	60	z-cut quartz	2.027	133	4.030	84	1.50
3	1s-1475	100	z-cut quartz	2.030	131	4.037	82	1.46
4	1s-1434	200	z-cut quartz	2.025	131	3.899	82	1.46

to mitigate radial release for these experimental conditions. The copper targets are prepared as right circular cylinders 15 mm in diameter and 4 mm in nominal thickness. Three concentric momentum trapping rings, also made of 4 mm thick annealed copper, are pressed fit around the sample to mitigate perturbations from edge release waves. Since the sample diameter in these experiments is only 15 mm, two additional rings are used to decrease the likelihood that edge waves would reach the sample. Furthermore, the sample and inner ring are machined with a 7° taper to ensure that the sample will separate from the rings. After press-fitting the sample and rings, the assembly is lapped flat and parallel to a tolerance of $5 \mu\text{m}$ and glued into a target plate. Several diagnostic pins are positioned around the perimeter of the target assembly to measure the impactor velocity, tilt, and to trigger diagnostic equipment. After assembly, the parallelism, of the sample to the target plate, and the height of each pin with respect to the target plate are measured. Velocity profiles are obtained using a VISAR probe (spot size $\sim 0.5 - 1$ mm diameter) mounted 90° off of the shock direction axis to prevent impact with the probe. In all cases shots are performed between two and four times to test repeatability as well as generate statistically accurate measurements of damage distributions.

2. Postimpact metallurgical characterization

Subsequent characterization of the damage in the spalled samples include optical and EBSD microscopy. In addition, micro x-ray tomography is used to reveal the 3D view of the damage fields. In preparation for the optical and EBSD analyses, each recovered specimen is diametrically sectioned. They are subsequently mounted in an epoxy resin and prepared following standard metallographic techniques up to a $0.05 \mu\text{m}$ colloidal silica final polish, performed on a vibratory polisher. Finally, they are electrochemically polished using a solution of two parts of phosphoric acid to one part water at ~ 1.9 V for ~ 10 s. A similar procedure is followed on the undeformed, as-annealed samples. Optical microscopy was performed on a Zeiss microscope equipped with an automated stage. Image processing is done using Image J. EBSD is performed on a Phillips XL30 FEG SEM using a voltage of 20 kV and a spot size of 4, with varying step sizes of 0.25 to $1.5 \mu\text{m}$, depending on the feature of interest.

In preparation for micro x-ray tomography, prismatic samples are obtained from the central region of the recovered samples with dimensions ~ 2 mm wide and thick, and ~ 4 mm in height. The samples are analyzed with an Xradia microcomputed x-ray tomography (MXCT) instrument,

which uses a Hamamatsu tungsten microfocus x-ray source ($5 \mu\text{m}$ nominal spot size). Samples are run at 150 kV and 10 W. The source is covered with two glass slides to reduce beam hardening. Using the $10\times$ objective with a 2 mm field of view, the entire cross section of the piece was imaged. One-minute exposures of 1261 images³¹ (184° total rotation) were collected on the $2k \times 2k$ CCD detector which was binned so that each image was $1k \times 1k$. Reconstruction of the data is performed using XMRConstructor. Post image analysis is performed using Avizo Fire Version 6.2. The analysis routine is discussed elsewhere.³²

III. RESULTS

A. Free surface velocity profiles

Figure 4(a) shows the free surface velocity (FSV) histories for the experiments reported herein. Key parameters are listed in Table I. The peak free surface velocities range from 82–84 m/s, corresponding to peak compressive stresses of 1.46 – 1.50 GPa. These values are calculated using the Mie Grüneisen equation of state for copper: $\rho_o = 8.924 \text{ g/cm}^3$ (density), $C_o = 3.94 \text{ mm}/\mu\text{s}$ (bulk sound speed), $s = 1.489$ and $\gamma = 1.96$. Figure 4(b) shows the free surface velocity histories once significant yielding begins causing a drop in the free surface velocity [marked by a red rectangle in Fig. 4(a)]. The times and velocities are shifted so that the drop from the peak state starts at $t = 0$. From these results and using the approximation:

$$\dot{\epsilon} \equiv \frac{1}{2C_o} \frac{dFSV}{dt} \quad (1)$$

derived from the $\epsilon - V/V_o$ and $V/V_o - u_p$ relationships found in Ref. 33 a tensile strain rate ($\dot{\epsilon}$) of approximately $0.8 \times 10^5/\text{s}$ is estimated in all cases.

The spall strength (σ_{spall}) is calculated using the relationship in Ref. 34 for a material that exhibits an elastoplastic behavior:

$$\sigma_{spall} \equiv \rho_o C_L \Delta FSV \left(1 + \frac{C_L}{C_o} \right)^{-1}, \quad (2)$$

where $C_L = 4.77 \text{ mm}/\mu\text{s}$ is the longitudinal sound speed and ΔFSV is the difference in free surface velocity from the peak state to the minima. The measured and calculated key parameters are listed in Table II. It is found that by holding the loading profile constant (i.e., peak stress and tensile strain rate are the same for each experiment), the calculated spall strength is $\sim 1.31 - 1.38$ GPa (Table II), with no clear effect of the grain size on the value.

Nevertheless, differences are observed in the magnitude and rate at which the velocity rises to the first peak (i.e., spall peak) beyond the minima. Figure 4(c) shows the region of interest in the free surface velocity profiles [red rectangle in Fig. 4(b)]. Again, the times and velocities are shifted so that the minima coincides with the origin in the plot. For experiments of grain sizes larger than 30 μm , it is observed that the magnitude of the spall peak and the acceleration rate increases with increasing grain size. In a qualitative manner and following a similar framework laid out by Cochran and Banner,³⁵ the ratio of the spall peak velocity ($V_{\text{sp-pk}}$) with respect to the peak velocity is found to be proportional to the void density existent in the sample. Table II lists the ratio of these velocities for the current experiments. These ratios are then correlated to the amount of damage in the samples, hence an increasing damage content (void area fraction) for Exps. 2, 3, 1, and 4 (60, 100, 30, and 200 μm , respectively), from least to greatest, is expected prior to the metallographic analysis.

Furthermore, in ductile materials, the rate at which the velocity rises is generally related to the void growth rate. In simulations found in Ref. 1, the acceleration in the free surface velocity is correlated with the velocity gradient of the wave reflected off the spall plane. The velocity of this wave varies from C_L , in cases where there is a rapid fracture process; to C_0 in the cases where there is a stress relaxation due to a resistance to void growth, rendering lower damage rates.³⁶ Thus, shorter rise times to the spall peak correlate with a more rapid completion of the damage. In addition, Fig. 4(c) shows that the 30 and 200 μm samples exhibit a monotonic rise from the minima to the spall peak, while the 60 and 100 μm samples show a distinctive change in slope. Table II lists the measured rise times from the pullback minima to the spall peak ($\Delta t_{\text{sp-pk}}$). The rise times follow similar trend as the spall peak velocity values with respect to the grain size, therefore, the degree of damage development, in the form of larger average void size, is expected to increase in the same order as the damage content: 60, 100, 30, and 200 μm .

However, because the previous inferences are based entirely on interpretations of the measured free-surface velocity histories, and because of the inherent problems of this type of measurement, such as probe size, characterization of incipiently spalled samples is performed to gain insight into the physical nature of the damage evolution as a function of grain size in copper.

B. Postimpact characterization

The primary objective of the present work was to conduct a careful postimpact examination of the recovered samples to develop a statistical representation of the damage characteristics. The results presented in this section include optical, EBSD and micro x-ray tomography observations that illustrate the damage characteristics.

1. Optical analysis

Figures 5(a)–5(d) show the bright field, optical micrographs of the cross sections of the recovered samples. Due to

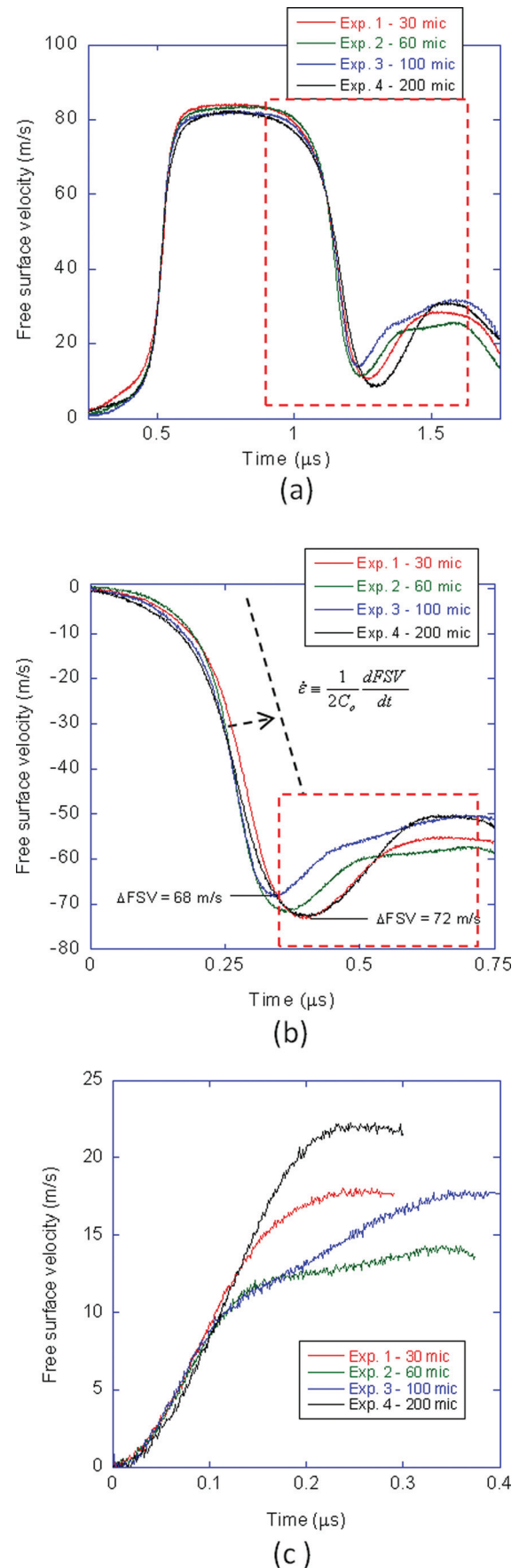


FIG. 4. (Color) (a) Free surface velocity histories, (b) Pull-back wave, for the four different grain sizes, (c) free surface velocity after the minima.

TABLE II. Calculated values from free surface velocity traces.

Exp. No.	ΔFSV	Spall Strength σ_{spall}	Spall peak velocity V_{sp-pk} (m/s)	Ratio $V_{S_{sp-pk}}/V_{pk}$	Δt_{sp-pk} (μs)
1	72	1.38	18	0.214	0.241
2	71	1.36	14	0.167	0.349
3	68	1.31	17.5	0.208	0.345
4	72	1.38	22	0.262	0.231

the shock compression and subsequent tension to which the samples are subjected, the thickness of each recovered sample shows a slightly different value with respect to the original thickness. Figures 5(e)–5(h) show the processed images after being converted to 8 bit, binarized, and cleaned using Image J software. The voids are clearly distinguished as white spots on a black background. Qualitatively, an increasing amount of damage with increasing grain size is observed. The results from Exp. 1 clearly deviate from this trend showing a greater amount of damage than Exp. 2 and 3, and slightly less damage than Exp. 4, in agreement with the magnitude of the respective spall peak. The void shape/size is also differs as a function of grain size. While they remain small and round for Exp. 2, they appear bigger and more elongated as the grain size is increased, indicating that growth and/or coalescence has already begun.

The results from the quantitative analysis are listed in Table III and plotted in Fig. 6. Figure 6(a) shows the statistical results from all the experiments performed in this study. Beyond a grain size threshold (somewhere between 30 and 60 μm , as marked by the arrow), a clear linear trend is observed, with the void area fraction increasing with increasing grain size. Figure 6(b) shows the distribution of the void sizes, where this trend is also observed. In Exp. 2 the voids remain less than $\sim 75 \mu m$ in size, in Exp. 3 some voids are larger with sizes up to $\sim 100 \mu m$, and for Exp. 4 voids are largest with sizes of about $\sim 150 \mu m$. For the case of Exp. 1,

several large sized voids ($> 100 \mu m$) are observed. This behavior will be discussed in the next section.

2. Electron backscatter diffraction (EBSD) analyses

Figures 7(a)–7(d) show the orientation maps of the selected areas shown in the optical micrographs [Fig. 5(a)–5(d)]. Voids preferentially nucleate along grain boundaries, the defect of interest in this study, with no clear correlation between grain orientations and void nucleation sites. Figures 7(b)–7(d) confirm the optical observations that in the sample from Exp. 2 voids remained small and isolated. On the contrary, void growth and coalescence become more predominant for Exps. 3 and 4, rendering larger voids as the grain size increases. Figure 7(a) elucidates the behavior exhibited by the sample from Exp. 1. In this specimen too, voids tend to nucleate at grain boundaries. However, the nature of the grain boundary distribution in this smaller grained specimen is such that voids nucleate in relatively close proximity to one another and coalescence is therefore promoted (as indicated by the arrows). As a result the large voids captured during the optical analysis, are in reality groups of small voids coalesced to form bigger voids.

To further investigate the effect of the grain size on the damage characteristics, higher magnification orientation maps along with their respective average kernel misorientation maps are shown in Fig. 8. The average kernel

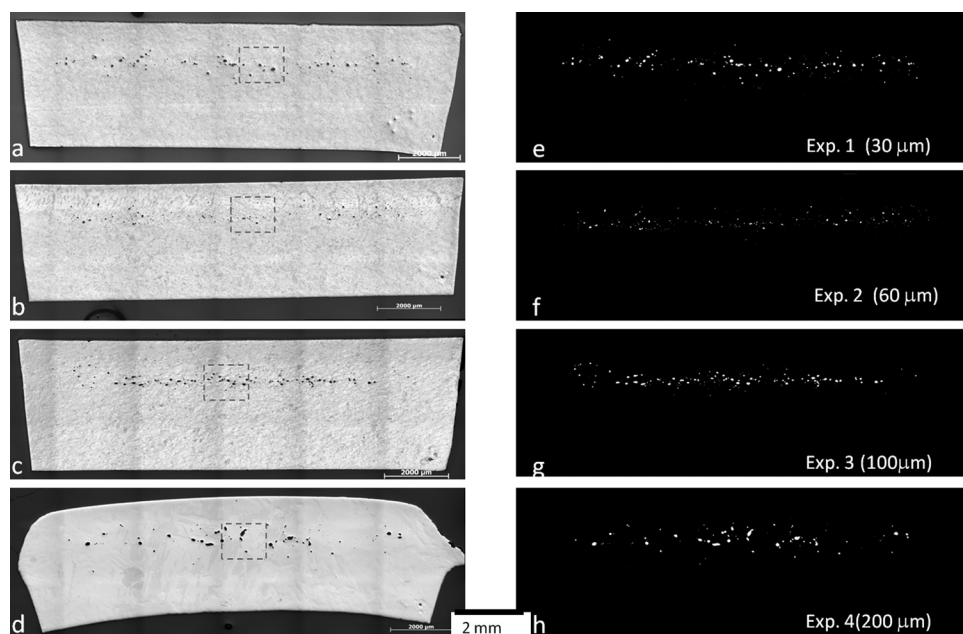


FIG. 5. Optical micrographs of the cross sections of the recovered: (a)–(d) bright field images of Exp. 1–4, respectively, (e)–(h) processed images.

TABLE III. Damage statistics from optical analysis.

Exp. No.	Grain Size (μm)	Number of Voids	Area Fraction (%)	Average Void diameter (μm)
1	30	236	0.496	38.1
2	60	343	0.249	22.7
3	100	267	0.416	33.0
4	200	111	0.507	55.1

misorientation is an approach used to correlate plastic deformation to a microstructural misorientation.³⁷ The misorientation maps show highly localized deformation fields around already coalesced voids for Exps. 1, 3, and 4, while the sample from Exp. 2 shows zones of relatively high misorientation linking voids, which have not yet coalesced. A result that suggests that some of the energy supplied by the shock could have been dissipated by plastic work and resulted in misorientation tracked in Fig. 8(f). This left less energy available for void growth and eventual coalescence that is observed in Exps. 1, 3, and 4 [Figs. 8(e), 8(g), and 8(h)].

Figures 9 and 10 show several types of maps calculated from EBSD data. These include: Taylor and Schmid factors, elastic stiffness, and special grain boundary types for samples from Exps. 3 and 4. They aided in establishing deterministic trends for void nucleation. The analysis is summarized as follows:

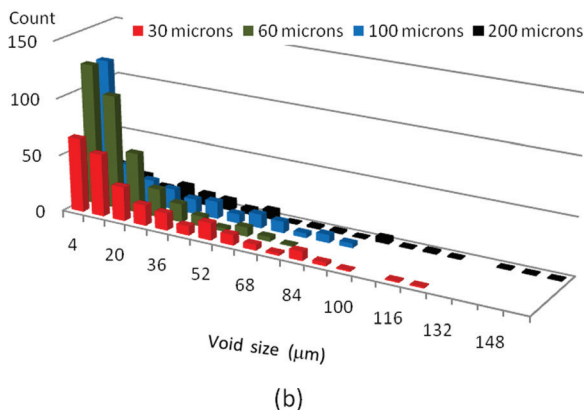
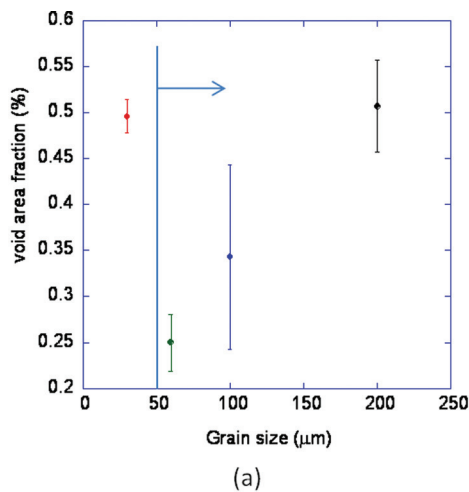


FIG. 6. (Color) (a) Void area fraction as function of the grain size, (b) void size distribution.

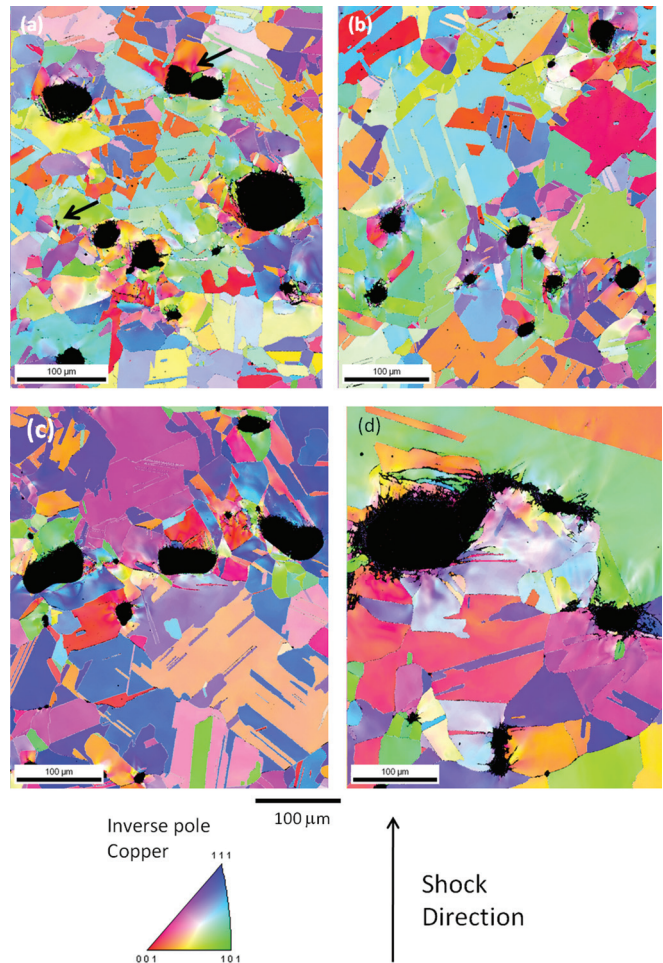


FIG. 7. (Color) EBSD orientation maps (IPF) of the selected areas in Fig. 4: (a) Exp. 1, (b) Exp. 2, (c) Exp. 3, (d) Exp 4.

a. Taylor factor (TF), Schmid factor (SF), and elastic stiffness (ES). For all of the cases analyzed, there was no clear correlation between void location and differences in either Taylor/Schmid factors, or elastic stiffness across grain boundaries containing voids [Figs. 9(a)–9(d) and 10(a)–10(d)]. For instance, in Figs. 9(b) and 10(b) it is observed that adjacent grains, as signaled by the white arrows, with the largest difference in Taylor factors (blue and red being the minimum and maximum, respectively), seem to be resistant to void nucleation at their grain boundary. However, in the same area, as indicated by the green arrows in Fig. 10(b), boundaries with similar differences in these values nucleated voids.

b. Grain boundary type. It is observed for all cases that voids are not nucleated at special grain boundaries, specifically the $\Sigma 1$ and $\Sigma 3$ types that correspond to low and 60° misorientation angle, respectively. The misorientation profiles across grain boundaries containing voids confirm the previous observations [Figs. 9(f) and 10(f)]. For all the cases analyzed, the misorientation angles of grain boundaries containing voids are in the range of $\sim 15^\circ$ – 55° . As additional evidence of this phenomenon, in Fig. 11, are presented the results from a large grained copper sample incipiently damaged in a concurrent study. As show in Fig. 11(a), the sample

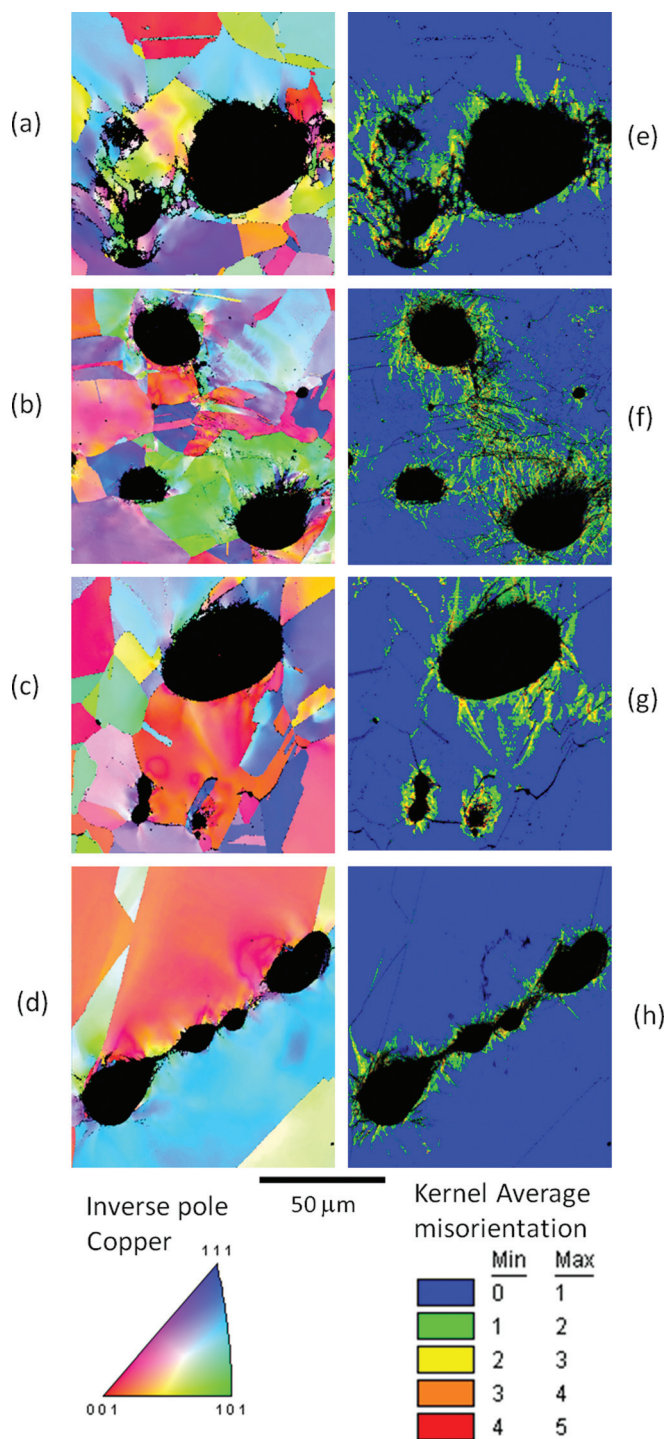


FIG. 8. (Color) High magnification orientation (a)–(d) and average kernel misorientation (e)–(h) maps of Exps. 1–4, respectively.

had a five columnar-grained structure, so the analysis of the slice shown in Fig. 11(b) presented a great opportunity to test the validity of our observations: it contains three grains and hence two grain boundaries, one being a $\Sigma 3$ and the other a high angle grain boundary ($\sim 50^\circ$). Figures 11(c) and 11(e) show that the $\Sigma 3$ boundary was able to withstand the uniaxial tensile stress (with a significant hydrostatic component), while the high angle boundary failed [Figs. 11(d) and (f)] at similar stress.

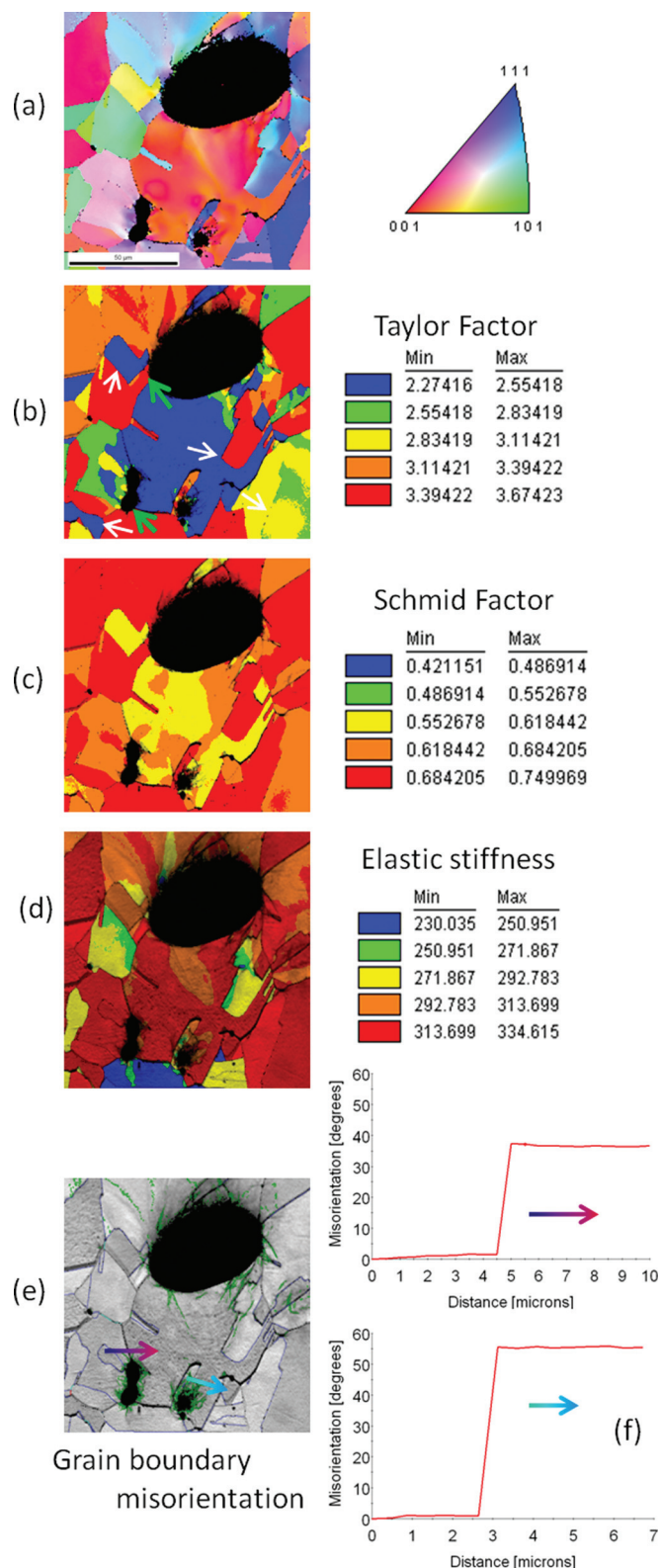


FIG. 9. (Color) Calculated properties from the EBSD data collected on the samples from Exp. 4. (a) Orientation map, (b) Taylor factor, (c) Schmid factor, (d) elastic stiffness, (e) CSL boundaries, (e) misorientation profiles as indicated by the arrows.

3. Micro x-ray tomography measurements

Figure 12 shows three-dimensional views of the damage field in the recovered samples. These results qualitatively confirm and lend statistics to the optical and EBSD observations.

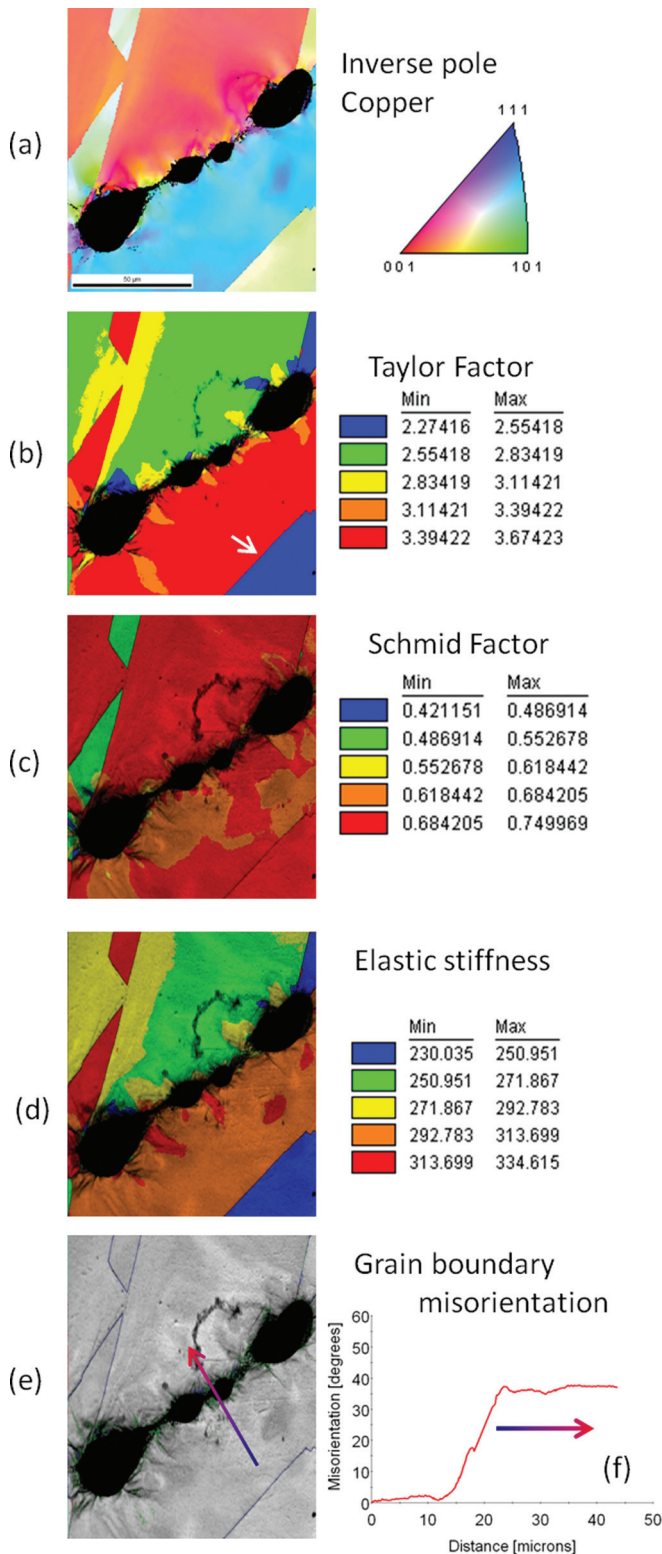


FIG. 10. (Color) Calculated properties from the EBSD data collected on sample from Exp. 3. (a) Orientation map, (b) Taylor factor, (c) Schmid factor, (d) elastic stiffness, (e) CSL boundaries, (f) misorientation profiles as indicated by the arrows.

The measured 3D damage content and void size correlated with the two-dimensional observations. A proper approach for a reliable quantitative analysis is currently under investigation.²⁵ As a preliminary and promising result, the void volumetric fraction (V_V) was calculated gravimetrically to be

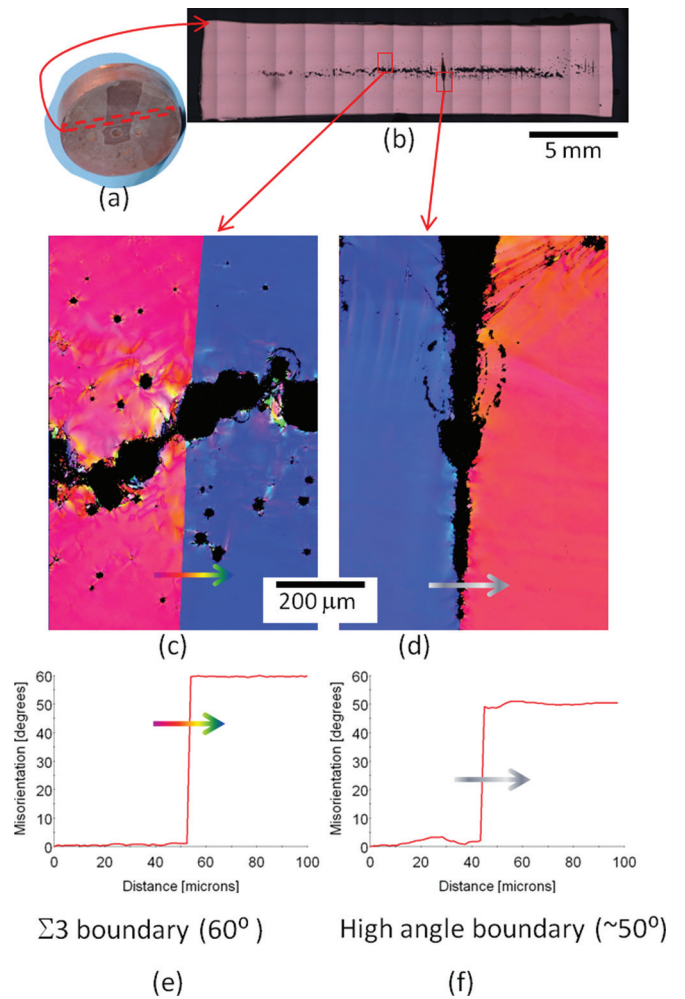


FIG. 11. (Color) Results from a columnar grained Cu sample. (a) Sample, (b) optical micrograph of the cross section, (c)–(d) Orientation maps of the selected areas. (e)–(f) Misorientation profiles as indicated by the arrows.

0.42% for the sample from Exp. 3. This is in agreement with the estimated value of 0.41% for the void area fraction (A_A), obtained from analysis of 2D micrographs, and provides a remarkable experimental confirmation of the stereological relationship $A_A = V_V$, normally assumed when trying to assess the volumetric characteristics of a property (i.e., damage) from 2D measurements. Tomographically, summing the volume of all voids yields a total void volume of 0.64%. The discrepancy arises due to the size of the areas analyzed. The analyses in 2D involve measurements based on the entire cross sections of the recovered samples, while the tomography measurements are done on smaller regions containing a higher amount of damage (Sec. II B 2). A study to improve 3D image segmentation accuracy is underway.

IV. DISCUSSION

As presented in Sec. III A, the same loading conditions are applied in all experiments: peak stress, pulse duration, and strain/strain rate or release rate were held constant. Under these conditions, it is found that the value for the onset stress for spall remains similar with no evident effect of the grain size. It should be noted that this type of calculation is ambiguous because it represents a continuum level

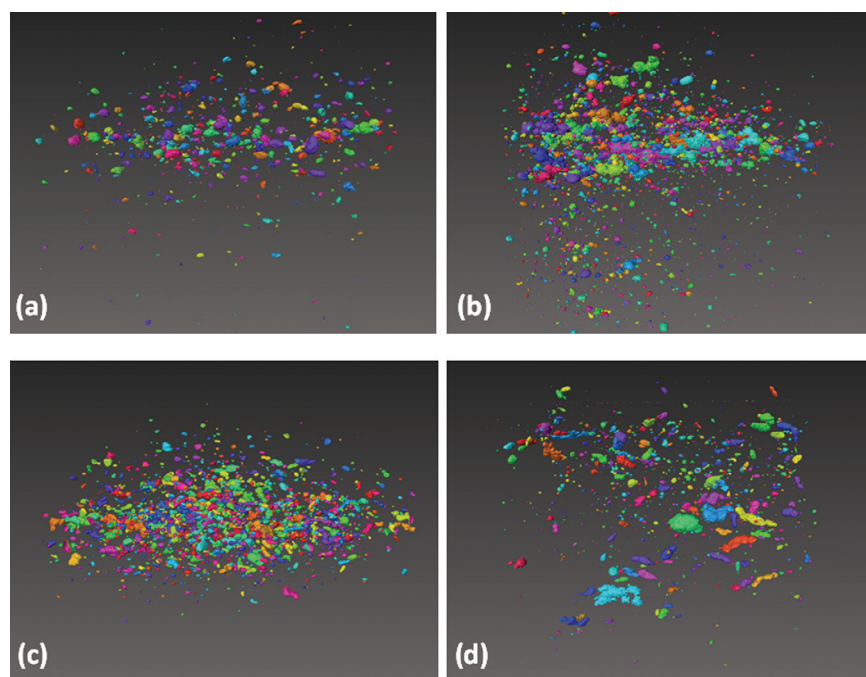


FIG. 12. (Color) Micro x-ray tomography results for: (a) Exp. 1, (b) Exp. 2, (c) Exp. 3, (d) Exp. 4. The color holds no physical significance other than allowing to distinguish between individual voids.

measurement of the convolution of all physical processes resulting in the overall dynamic response of the material being tested.

Drawing conclusions from continuum level measurements such as free surface velocity and correlating them to the mesoscale microstructural processes is accomplished through careful model driven experimental design coupled with metallographic analysis of recovered test materials. In particular, it has been found that the characteristics of the free surface trace after the pull-back minima reflects the material behavior and can be used as an indicator of the magnitude and characteristics of the resultant damage.^{14,35,38} In this context, our results show good agreement between the measured free surface velocity traces and the postimpact characterization, as a function of the grain size. The higher the ratio of peak state to spall peak, the higher the void fraction was observed in the respective sample. Similarly, the free surface velocity acceleration after the pull-back minima correlate with void growth mechanism, in which higher rates rendered larger voids indicative of coalescence rather than growth of individual voids. Interestingly, the samples that show a change in slope in the free surface velocity after the minima, present higher average kernel misorientations (Exp. 2). This is indicative of the competition between void growth and plastic dissipation processes that is captured in the free surface velocity measurements.

From the EBSD analyses it is established that the voids preferentially nucleate at grain boundaries other than the special $\Sigma 1$ and $\Sigma 3$ boundaries. This confirms the importance of strictly controlling and characterizing the fraction of these boundaries, as emphasized in Sec. II A for any damage study investigating microstructural influence. Similar observations have been recently reported by Peralta and co-workers^{17,19} on Cu samples deformed in laser-driven spall experiments. Although the loading conditions (i.e., peak stress, pulse duration, strain rates) and experimental length scales differed

with respect to the experiments performed in the current study, their results aid to establish that void nucleation has some deterministic features, and the location of damage may be linked to intrinsic properties of the grain boundaries. At the moment, MD simulations are being performed to elucidate if the resistance to void nucleation of the special $\Sigma 3$ boundaries is a matter of cohesive strength and/or lattice coherence between neighboring grains that would allow for dislocation migration across them, therefore, precluding dislocation pile-ups normally seen as precursors for void nucleation.^{39,40}

In what follows, we present a series of mechanisms that attempt to explain the metallographic and free surface velocity trace observations.

A. Phenomenological mechanisms for void nucleation and early growth and coalescence as function of the grain size

Figure 13(a) schematically illustrates the initial configurations for the four cases of early damage evolution corresponding to the experiments examined in this study. Colored in red are grain boundaries, excluding the $\Sigma 1$ and $\Sigma 3$ types that may act as potential nucleation sites. It should be noted that the rest of the area (or volume) is filled with the $\Sigma 1$ and $\Sigma 3$ boundaries. As depicted in Fig. 13(a), with increasing grain size a given volume has fewer potential nucleation sites, but each site becomes larger.

As the region of tension develops in the test materials, voids are nucleated and grown at some of the potential sites. A grain boundary other than $\Sigma 1$ or $\Sigma 3$ is a necessary but not sufficient condition to nucleate voids. Figures 13(b) show that the number of voids being nucleated is comparable for all cases due to similar loading conditions and relatively similar defect density (slightly decreasing with increasing grain size, Sec. II A).

As tension progresses, Figs. 13(c) illustrates that the proximity of the nucleated voids gives rise to either individual growth of isolated voids or coalescence depending on whether or not they are within some critical separation distance. Hence, void coalescence will be enhanced in samples with relatively small grain sizes ($30\ \mu\text{m}$ in this study) in which voids were nucleated on different grain boundaries and are close together, or on samples with large grain sizes ($200\ \mu\text{m}$) in which several voids were nucleated along the same grain boundary and are close together. On the contrary, in samples with intermediate grain sizes (60 and $100\ \mu\text{m}$), the voids will tend to grow but remain isolated for the most part, with some of the energy supplied by the load being lost as plastic work dissipation. It is suggested here, based on the observations of this study, that the differences in the growth of individual voids versus coalescence behavior of near neighbor voids result in the observed differences in the damage fields, and the similarities in the total damage fraction (void volume fraction) in the 30 and $200\ \mu\text{m}$ cases.

B. Effect of the damage evolution on the free surface velocity characteristics

Although energy dissipation in polycrystalline metallic materials is a complex phenomenon,^{41–43} a simplified energy argument is offered here to assist in understanding the present results while more sophisticated mesoscale modeling tools are developed to better couple the processes involved in nucleation, growth and coalescence of voids.

The acceleration in the free surface velocity after the minima can be related to the damage rate in the following simplified form, obtained from the one found in Refs. 1 and 44:

$$\frac{dFSV}{dt} \equiv A(\dot{V}_v - B), \quad (3)$$

where \dot{V}_v is the void volume rate, i.e., damage growth rate, and A and B are combinations of parameters corresponding to the density, strength and acoustic properties of the material. To incorporate the effect of grain size on the damage

growth and its subsequent effect on the free surface velocity trace, the mechanism proposed in the prior section is revisited with the focus on a given void and its closest neighbor. After the void is nucleated it starts to grow, with the growth behavior dictated by the competition of tensile and compressive stresses that results from the compressive and rarefaction waves [Fig. 14(a)]. In a similar framework as Irwin's model for crack growth in ductile materials,^{45,46} if the tensile stress exceeds the compressive stress, there is a net effective stress that causes the development of a plastic zone at the boundary of the growing void [Fig. 14(b)], with the size of the plastic region dependent on the applied stress and the material strength (toughness). The energy supplied by the effective stress can be divided into plastic dissipation (E_p), remote from the growing void, and plastic dissipation surrounding the growing void (E_{gv}). Hence the available energy for void growth can be calculated as:

$$E_{gv} = E_{\text{Total}} - E_p \cong CV_v, \quad (4)$$

where C is a proportionality constant relating void volume and the energy spent for its creation. In the case where plastic flow localizes around the growing voids, i.e., coalescence, most of the driving energy is dumped into void growth to cause a very rapid void growth.

In our experiments, by having similar loading conditions, the compressive and rarefaction stresses developed are similar in all of our samples, providing a close-to-constant total energy from sample to sample. Physically this means that, in comparing our samples, those with more plastic dissipation loss will have a lower void growth rate and a, consequently, lower acceleration rates in the free surface velocity rate. It should be noted that similar conclusions were obtained by Cochran and Banner,³⁵ in which the steeper the free surface velocity was related to a more brittle behavior in the material, i.e. less plastic dissipation. In our case, plastic dissipation is promoted in microstructures in which there is more volume allowing for plastic deformation, such as the $60\ \mu\text{m}$ case [Figs. 14(b)]. However, as

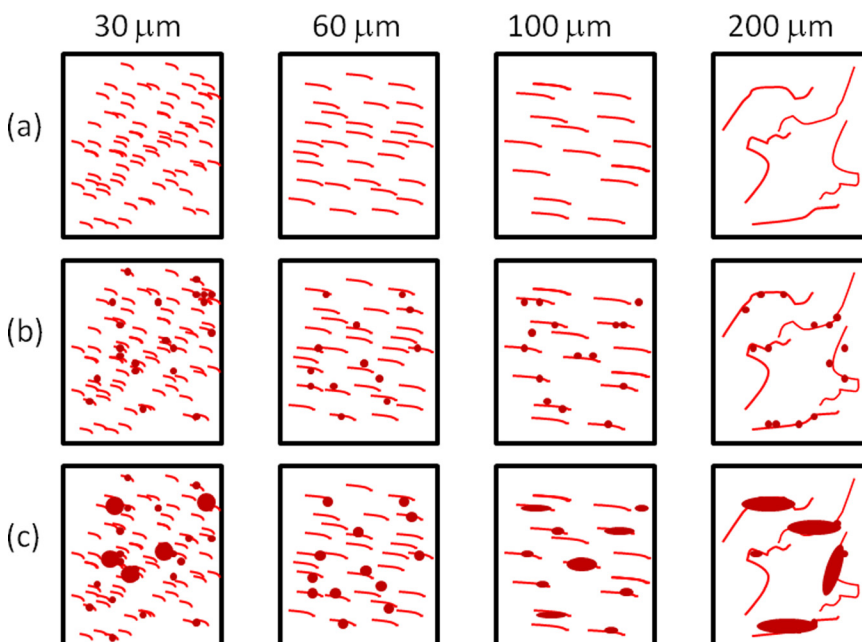


FIG. 13. (Color online) Mechanisms proposed: (a) initial configuration of the grain boundaries $\neq \Sigma 3$, (b) microstructure during void nucleation stage, (c) resultant microstructure after void growth plus coalescence.

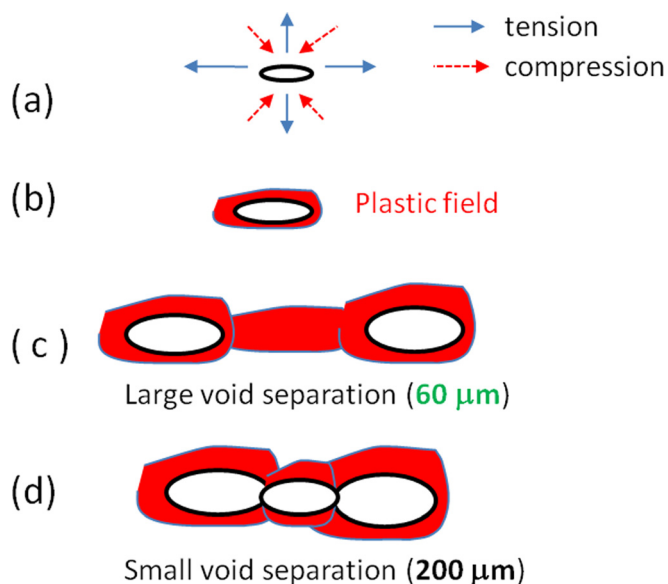


FIG. 14. (Color online) Analogous Irwins' model for damage growth. (a) Stress state, (b) development of plastic field. Void separation dictating: (c) plastic dissipation vs (d) coalescence.

mentioned earlier, if coalescence exists due to the presence of a near neighboring growing void and its associated plastic field (30 or $200 \mu\text{m}$ cases), the remote plastic work will cease at the moment of coalescence, causing a decrease in the remote plastic dissipation rate, in turn, accelerating the void growth rate and inherently accelerating the rate of the free surface velocity. As previously stated, these phenomena are reflected in the free surface velocity traces where there is a correlation between higher acceleration rates after the minima and large sized voids that resulted from coalescence (30 and $200 \mu\text{m}$).

V. SUMMARY

Plate impact experiments were conducted to examine the effect of grain size on the dynamic tensile response of copper samples. By holding the shock loading conditions constant (peak stress, pulse duration and strain rate) it was possible to elucidate the spatial effects (grain size) on the dynamic tensile response of copper samples. Characterization of the initial microstructures and the incipient damage was performed using optical and EBSD microscopy along with micro x-ray tomography. The main findings are as follows:

- The free surface velocity traces do not show a clear effect of the grain size on the shock rise, compression, release and calculated spall strength. However, differences are observed in the characteristics of the pull-back signal beyond the minima. The magnitude of the spall peak and the rate at which the free surface velocity rises to achieve it, are clearly dependent upon the grain size and are correlated to growth mechanism (i.e., coalescence dominated or isolated void growth).
- The quantitative metallographic analysis showed good agreement with the inferences made from the free surface velocity measurements and the damage characteristics observed in the recovered samples. A higher spall peak correlated with a

larger void area fraction observed in the respective recovered sample. Similarly, the acceleration rates correlated with the void shape/size observed in the damage field of the recovered samples resulting in identification of dominant growth mechanism (i.e., coalescence or individual void growth).

- EBSD analyses aided to establish that the grain boundary type was the dominant factor in determining the preferred void nucleation sites. In particular, a grain boundary other than the special $\Sigma 1$ or $\Sigma 3$ boundary was found to be a necessary, but not a sufficient, condition for void nucleation. Additional work is currently being performed to establish any other necessary condition, and if the tendency of the $\Sigma 3$ boundaries to avoid void nucleation is a matter of cohesive strength and/or lattice coherence between neighboring grains that would allow for dislocation passage.
- By focusing on the grain boundaries that could act as nucleation sites, it was proposed that the number of voids being nucleated is similar, therefore causing a similar decrease in the mass impedance, translated to comparable values for the calculated spall strength. However, the void growth and coalescence behavior are clearly dependent on the spatial distribution and size of the defects (i.e., grain size), with coalescence being more dominant in the 30 and $200 \mu\text{m}$ samples.

From these findings it is concluded that the free surface velocity history after the pullback minima provides a direct indicator of the active mechanism of damage evolution. Initially, the rise after the minima (growth rate of voids according to Cochran and Banner) is fast as nucleation is occurring at grain boundaries other than $\Sigma 1$ and $\Sigma 3$. Grain size then contributes to material response by controlling the growth mechanism that becomes dominant after void nucleation occurs. A coalescence dominated growth mechanism (as observed in the 30 and $200 \mu\text{m}$ samples) is indicated by a continuation of a steep acceleration slope after the minima beyond the nucleation region. This is the transition that allows for a monotonic rise to the spall peak as observed. A growth mechanism that is not dominated by coalescence, where individual voids must grow with the concomitant plastic dissipation, is indicated by a transition to a much more shallow acceleration to the spall peak. This transition is observed in the 60 and $100 \mu\text{m}$ samples. It is also worth noting that as coalescence begins (even when individual void growth continues to be dominant) the overall void growth rate increases. It is expected that as more coalescence is observed, steeper acceleration slopes to the spall peak will also be observed until the point at which coalescence dominates (as observed in the 30 and $200 \mu\text{m}$ samples).

This study helps to address some of the contradictory information regarding the effect of grain size on dynamic response of materials by carefully maintaining a constant volume of material sampled in the tensile region during the experiment. This allows us to vary the grain size within that volume directly to probe the mesoscale effects responsible for the observed continuum level results. Consequently, the findings reported herein might aid in the explanation of contradictory results regarding the effect of the grain size on the calculated spall strength found in other incipient spall

damage studies within the literature. It might be possible, that not only the grain size was changed but also the fraction of the special grain boundaries ($\Sigma 1$ or $\Sigma 3$). If a strict control of this property is not followed, and based on our observations, we conjecture that a Hall–Petch-type behavior would be observed in which the fraction of special grain boundaries significantly decreased with increasing grain size, hence significantly increasing the number of potential nucleation sites.

In addition, the experimental results presented here constitute a valuable reference for validation of any model that attempts to correlate microstructure and ductile damage evolution. Such formulations, which combine crystal plasticity and dilatational plasticity, including models for nucleation, growth and coalescence of voids in a polycrystalline matrix, have recently been developed.⁴⁷ Comparison with observations from the present experiments is underway and will be reported. Finally, experiments on microstructures similar to those presented here at higher compressive stresses, where complete spall is achieved, would be helpful to gain insight into the physical meaning of the spall strength parameter. In these experiments, the calculated spall strength is directly related to the overall resistance to create a new surface. Thus, we anticipate that it will become a percolation problem in which the strength will be related to the ability to create a connected region of damage, with transgranular fracture being more significant with increasing grain size. In other words, we anticipate an inverse Hall–Petch behavior, with the spall strength increasing with increasing grain size.

ACKNOWLEDGMENTS

This work was supported by LDRD-DR 20100026. The authors would like to thank Mike Lopez for his help with the heat treatment of the samples and Ruben Manzaneres for his help with assembly. John Bingert and G. T. “Rusty” Gray are also gratefully thanked for the fruitful discussions during the preparation of this manuscript.

- ¹T. Antoun, L. Seaman, D. Curran, G. Kanel, S. Razorenov, and A. Utkin, *Spall Fracture* (Springer, New York, 2002), p. 26.
- ²L. M. Barker and H. Re, *J. Appl. Phys.* **43**, 4669 (1972).
- ³O. T. Strand, D. R. Goosman, C. Martinez, T. L. Whitworth, and W. W. Kuhlow, *Rev. Sci. Instrum.* **77**, 083108 (2006).
- ⁴W. F. Hemsing, *Rev. Sci. Instrum.* **50**, 73 (1979).
- ⁵R. S. Hixson, G. T. Gray, P. A. Rigg, L. B. Addessio, and C. A. Yablinsky, *AIP Conf. Proc.* **706**, 469 (2004).
- ⁶G. T. Gray and C. E. Morris, *J. Phys.* **IV 1**, 191 (1991).
- ⁷J. N. Johnson, G. T. Gray, and N. K. Boume, *J. Appl. Phys.* **86**, 4892 (1999).
- ⁸D. D. Koller, R. S. Hixson, G. T. Gray, P. A. Rigg, L. B. Addessio, E. K. Cerreta, J. D. Maestas, and C. A. Yablinsky, *J. Appl. Phys.* **98**, 103518 (2005).
- ⁹J. N. Johnson, *J. Appl. Phys.* **52**, 2812 (1981).
- ¹⁰D. R. Curran, L. Seaman, and D. A. Shockey, *Phys. Today* **30**, 46 (1977).
- ¹¹T. W. Barbee, L. Seaman, R. Crewdson, and D. Curran, *J. Mater.* **7**, 393 (1972).

- ¹²L. Seaman, D. R. Curran, and D. A. Shockey, *J. Appl. Phys.* **47**, 4814 (1976).
- ¹³M. A. Meyers and C. T. Aimone, *Prog. Mater. Sci.* **28**, 1 (1983).
- ¹⁴R. W. Minich, J. U. Cazamias, M. Kumar, and A. J. Schwartz, *Metall. Mater. Trans. A* **35A**, 2663 (2004).
- ¹⁵R. W. Minich, M. Kumar, A. Schwarz, and J. Cazamias, *AIP Conf. Proc.* **845**, 642 (2006).
- ¹⁶A. J. Schwartz, J. U. Cazamias, P. S. Fiske, and R. W. Minich, *AIP Conf. Proc.* **620**, 491 (2002).
- ¹⁷P. Peralta, S. DiGiacomo, S. Hashemian, S. N. Luo, D. Paisley, R. Dickerson, E. Loomis, D. Byler, and K. J. McClellan, *Int. J. Damage Mech.* **18**, 393 (2009).
- ¹⁸D. L. Tonks, J. Bingert, V. Livescu, and P. Peralta, *AIP Conf. Proc.* **1195**, 1081 (2009).
- ¹⁹L. Wayne, K. Krishnan, S. DiGiacomo, N. Kovvali, P. Peralta, S. N. Luo, S. Greenfield, D. Byler, D. Paisley, K. J. McClellan, A. Koskelo and R. Dickerson, *Scr. Mater.* **63**, 1065 (2010).
- ²⁰J. Buchar, M. Elices, and R. Cortez, *J. Phys.* **IV 1**, 623 (1991).
- ²¹W. R. Thissell, A. K. Zurek, D. A. S. Macdougall, D. Miller, R. Everett, A. Geltmacher, R. Brooks, and D. Tonks, *AIP Conf. Proc.* **620**, 475 (2002).
- ²²A. L. Gurson, *ASME J. Eng. Mater. Technol.* **99**, 2 (1977).
- ²³V. Tvergaard, *Int. J. Fract.* **17**, 389 (1981).
- ²⁴V. Tvergaard, *Int. J. Fract.* **18**, 237 (1982).
- ²⁵V. Tvergaard and A. Needleman, *Acta Metall. Mater.* **32**, 157 (1984).
- ²⁶E. N. Harstad, P. J. Maudlin, and J. B. McKirgan, *AIP Conf. Proc.* **706**, 569 (2004).
- ²⁷G. T. Gray, E. Cerreta, C. A. Yablinsky, L. B. Addessio, B. L. Henrie, B. H. Sencer, M. Burkett, P. J. Maudlin, S. A. Maloy, C. P. Trujillo, and M. F. Lopez, *AIP Conf. Proc.* **845**, 725 (2006).
- ²⁸G. T. Gray III, Influence of Shock-Wave Deformation on the Structure/Property Behavior of Materials, in *High Pressure Shock Compression of Solids*, edited by J. R. Asay and M. Shahinpoor (Springer-Verlag, New York, 1993), pp. 187.
- ²⁹A. L. Stevens and O. E. Jones, *J. Appl. Mech.* **39**, 359 (1972).
- ³⁰G. T. Gray III, Influence of Shock-Wave Deformation on the Structure/Property Behavior of Materials, in *High Pressure Shock Compression of Solids*, edited by J. R. Asay and M. Shahinpoor (Springer-Verlag, New York, 1993), pp. 187.
- ³¹B. M. Patterson and C. E. Hamilton, *Anal. Chem.* **82**, 8537 (2010).
- ³²B. P. Patterson, J. P. Escobedo, D. Dennis-Koller, and E. K. Cerreta, “Dimensional quantification of embedded voids or objects in three dimensions” *Microscopy and Microanalysis* (submitted).
- ³³G. R. Fowles, *J. Appl. Phys.* **32**, 1475 (1961).
- ³⁴G. I. Kanel, *J. Appl. Mech. Tech. Phys.* **42**, 358 (2001).
- ³⁵S. Cochran and D. Banner, *J. Appl. Phys.* **48**, 2729 (1977).
- ³⁶G. I. Kanel, S. V. Razorenov, A. V. Utkin, and D. E. Grady, *AIP Conf. Proc.* **370**, 503 (1996).
- ³⁷L. N. Brewer, D. P. Field, and C. C. Merriman, in *Electron Backscatter Diffraction in Materials Science* (Springer Science + Business Media, New York, (2009), p. 251–262.
- ³⁸J. P. Escobedo and Y. M. Gupta, *J. Appl. Phys.* **107**, 123502 (2010).
- ³⁹R. E. Rudd and J. F. Belak, *Comp. Mater. Sci.* **24**, 148 (2002).
- ⁴⁰J. Belak, *AIP Conf. Proc.* **429**, 211 (1998).
- ⁴¹R. Becker, *Int. J. Plast.* **20**, 1983 (2004).
- ⁴²T. J. Vogler and J. D. Clayton, *J. Mech. Phys. Solids* **56**, 297 (2008).
- ⁴³C. A. Bronkhorst, B. L. Hansen, E. K. Cerreta, and J. F. Bingert, *J. Mech. Phys. Solids* **55**, 2351 (2007).
- ⁴⁴G. I. Kanel and A. V. Utkin, *AIP Conf. Proc.* **370**, 487 (1996).
- ⁴⁵G. R. Irwin, *J. Appl. Mech.* **24**, 361 (1957).
- ⁴⁶G. R. Irwin, “Plastic zone near a crack and fracture toughness”, in *Proceedings of the 7th Sagamore Army Materials Research Conference*, edited by W. A. Backofen (Syracuse Univ. Press, Syracuse, N. Y., 1960), p. 63.
- ⁴⁷R. A. Lebensohn, M. I. Idiart, P. Ponte Castañeda, and P. G. Vincent, *Philos. Mag.* **91**, 3038 (2011).